MISR JOURNAL OF AGRICULTURAL ENGINEERING ISSN-Print: 1687-384X
https://mjae.journals.ekb.eg/ ISSN-Online: 2636-3062
Misr J. Ag. Eng., 40 (2): 139 - 160 **DOI:** 10.21608/mjae.2023.188580.1095

SIMULATION OF DESALINATION OF SALT WATER COMPRISING POLYPROPYLENE HOLLOW FIBRE MEMBRANES

Mahmoud M. Elewa[1], Omar Ramadan[2], Mahmoud A. El-Emam[3], Abdelaziz I. Omara[4]*

[1] Assoc. Prof. of Environ. Eng., Arab Academy for Science and Technology and Maritime Transport, Alexandria, Egypt.
[2] Assist. Prof. of Environ. Eng., Dept. of Architecture and Built Environ., U. of Nottingham, UK
[3] Assist. Prof of Ag. Power and Mach. Eng., Ag. and Biosystems Eng. Dept., Fac. of Ag., Alexandria U., Egypt.
[4] Assoc. Prof. of Ag. Irrigation and Drainage Eng., Ag. and Biosystems Eng. Dept., Fac. of Ag., Alexandria U., Egypt.

* E-mail: abdelaziz.omara@alexu.edu.eg

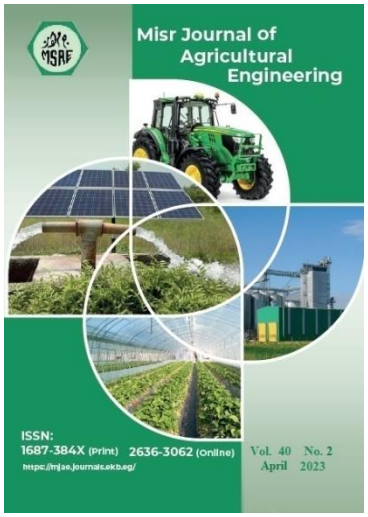

Keywords:
Water desalination; Humidification-Dehumidification; Hollow-fibre Membranes; Mathematical Model

ABSTRACT

The problem of desalination systems using advanced hollow fibre (HF) membranes were thoroughly investigated. Humidification air is cooled by heat transfer in the dehumidification chamber, which condenses the water vapour and produces high-quality, fresh drinking water. A mathematical approach was conducted, and a simulation programme (model) was developed for the system. The performance of the HF membranes was assessed using different mass flows of salt water and air to optimise the system's operating performance. An experimental setup was prepared to test the effect of changing the operating parameters on the produced fresh water's flux. The produced flux ranged from 2.36–10.6 kg h^{-1} m^{-2} at 40–70^{o}C, respectively. The comparisons between the simulation results and the experimental setup were in good agreement, and the water quality analysis showed that the obtained values were within the World Health Organization's drinking water guidelines.

1. INTRODUCTION

Rapid global population growth typically increases the demand for freshwater and reduces the capacity of many local supplies to provide freshwater (Arnot and Mattia, 2011). People struggle to balance decreasing per capita water supplies with rising population demands (Shatat *et al.*, 2013). Water spans over 71.0% of the earth's surface, and 97.5% is sea or brackish water, which is salty (Zhang and Li, 2017). Due to ongoing regional drought and migration of cities to coastal cities, water demand is expected to exceed supply by 56% by 2025. According to the United Nations, water scarcity could affect two to seven billion people could be affected by water scarcity over the next 50 years (Teow and Mohammad, 2019). The desalination system purifies brackish to produce freshwater with a total dissolved solids content of 500 ppm or less.

Conventional desalting systems such as electrodialysis (ED), reverse osmosis (RO), and distillation have several drawbacks, which consume substantial amounts of capital and energy

besides regular maintenance (Yang *et al.*, 2005; Welgemoed, 2006; Wang *et al.*, 2012). Different desalination plants include thermal processes with phase changes such as Multi-Stage Flash (MSF) (El-Dessouky *et al.*, 1996) and Multi-Effect Distillation (MED) (Sayyaadi and Saffari, 2010), membrane processes including RO (Gabelich *et al.*, 2007), hybrid methods with phase changes and membranes (Zhang and Li, 2017) have been developed to meet the demand for freshwater. However, such systems have economic limitations in remote areas, which require a considerable amount of energy as thermal steam (for MSF and MED) or electric power to maintain high mechanical pressure (for RO). Also, those desalination methods are suitable for large or medium-scale freshwater production (Li *et al.*, 2019). Residents in these remote areas need effective and alternative compacted or small-scale desalination plants with low energy costs to relieve the shortage of freshwater, which has been desirable in recent years by many countries.

In addition, using desalination technology integrated with renewable energy in freshwater production solves overcoming water shortages characterized by shortages of drinking water and traditional energy sources. Numerous studies on water desalination using the HDD process have recently been integrated with renewable energy. Sachdev *et al.* (2020) designed controlled simulations to predict the performance of HDD systems combined with wind towers and analysed the performance of the proposed system in terms of water production and thermal comfort. The results included a significant effect of inlet temperature on water productivity and an additional 10 to 12% water productivity in the closed-loop compared to the open-loop cycle. Elbassoussi *et al.* (2020) investigated the integration of an adsorption cooling/desalination cycle coupled with a water-heated HDD unit for freshwater production and cooling powered by natural gas with the addition of Photovoltaics (PV) to run the pumps and fans. The proposed system was modelled numerically. The obtained data concludes that the hybrid system provides a significant increase of 350% in the Gained Output Ratio (GOR) with a 30% to 40% reduction in water cost. Jabari *et al.* (2020) investigated the usage of a Stirling engine with a solar antenna with an HDD system to provide cooling, freshwater, and energy. The optimal operating point of the suggested system was determined using a generalized algebraic-mathematical modelling system (GAMS) and programs for engineering equation solving (EES).

Moreover, Chen *et al.* (2020) conducted an experimental study that combined an evaporative cooler with an HDD system. The system was found to have a GOR ranging from 1.6 to 2.4. The study also discovered that the proposed system's overall coefficient of performance (COP) outperforms the adsorption (AD) cooling/desalination systems (Qasem and Zubair, 2019), the absorption (AB) integrated chiller and the HDD cycle. Wang *et al.* (2020) carried out a mathematical model of a solar-powered air conditioning system combined with an HDD desalination unit. The solar component preheated regeneration air, and Phase Change Material (PCM) was also incorporated for heat storage. A typical day in August was used in the current study, and the main findings were that the optimum conditions achieved the COP of 0.411, the water production rate of 4.9 L h^{-1}, and the maximum thermal energy provided by the PCM component was 0.89 kWh.

On the other hand, He *et al.* (2019a) applied an open-air open-water (OAOW) HDD system for industrial waste heat recovery using mathematical modelling. The performance was

analysed in terms of energetic, entropic, and economic aspects. The optimum performance was calculated at a 96.45 kg h^{-1} water production rate and a GOR of 1.7. It was concluded that the increase in effectiveness would enhance the cost of water production and thermodynamic performance. He *et al.* (2019b) used thermodynamic modelling to investigate the integration of a heat pump with an OAOW HDD desalination system. The main findings concerned the GOR of the proposed system at various flow rate ratios, humidification effectiveness, and ambient humidity. The optimum water production rate was 150.75 kg $h^{-1,}$ and GOR was about 8.12 for the proposed integrated system. He *et al.* (2018) also carried out thermo-economic mathematical modelling with waste heat recovery. The unit cost of water production (UCWP) is decreased from \$40.35 kg^{-1} h to \$35.31 kg^{-1} h, with an increase in humidification effectiveness from 0.8 to 0.9. At the same time, the GOR increased from 1.28 to 1.85 with the rise of dehumidification effectiveness from 0.8 to 0.9 at the expense of higher cost.

Sharshir *et al.* (2016) assessed the performance of an HDD system integrated with four solar panels, reusing the HDD system's drain water to feed the stills through theoretical modelling. The GOR was found to increase by 50%, while the efficiency of solar still increased by 90%. The cost was \$0.034 per litre of produced water instead of \$0.049 in a conventional system. Elzayed *et al.* (2020) evaluated the performance of HDD using zero, single, and double extraction systems. Thermodynamic modelling was used to conduct this study, where the GOR of the system was found to be increased from 3.61 using zero extractions to 7.63 with double extractions and with 91% and 112% improvement in performance for single and double extractions compared to zero extraction system.

Several investigations have been conducted on integrating humidification systems with heat pumps. Ayati *et al.* (2019) performed a study on performing the integration of three different approaches, namely Variable pressure HDD (VPHDD), humidification compression (HC), and conventional HDD, with a heat pump (HP). According to this research, the VPHDD system provided superior performance to the other two methods, providing a water production cost of \$4.6/m^3. Furthermore, VPDHD performance was investigated by varying the dehumidifier to humidifier pressure ratio, humidifier pressure, and inlet water to air-mass flowrate ratio. Lawal *et al.* (2020)experimentally assessed the performance of an integrated HDD system powered by a heat pump. The system achieves a maximum GOR of 4.07, COP of 4.85, and capacity of 287.8 L/day while providing a cooling load of 3.07 kW.

Besides, Faegh and Shafii (2020) evaluated the performance of an HDD system combined with a heat pump employing an evaporative condenser. The performance was measured in terms of water production rate and GOR while operating parameters such as inlet air flow rate, compressor speed, and ambient wet-bulb temperature were varied. The best results were obtained with a water production rate of 1.08 kg h^{-1}, a GOR of 2, and a unit water production cost of \$0.019/L. Pourafshar *et al.* (2020) studied an HDD system combined with a heat pump and used a PVT sensor as the humidifier. The proposed design results in a unit water cost of \$0.018/kg.

Shehata *et al.* (2019) conducted an experimental study to determine the water production rate of an HDD desalination system. The impact of three major factors was analysed, including solar radiation, airflow rate, and water spray rates. In addition, Ultrasonic humidifiers were integrated to measure their impact on the water production rates. The maximum production

rate for water was 45 L Day^{-1} at an airflow rate of 0.46 kg s^{-1} and a spray rate of 0.3 for the tested system. Furthermore, the addition of an ultrasonic humidifier resulted in performance enhancement both in water production rate (9.3-14.6% at two different flow rates) and economically (decrease in costs per litre of produced water).

On the other hand, Al-Otoom and Al-Khalaileh (2020) experimentally investigated the impact of adding hygroscopic solutions containing Kaolin and $CaCl_2$ on the performance of the water desalination unit using a rotating belt. The study indicated that adding Kaolin to tap water improved the system's efficiency from 8.7% to 61% in the tests conducted in Jordan. Rahimi-Ahar *et al.* (2020) evaluated experimentally and theoretically the performance of vacuum HDD systems. The maximum desalination rate of 1200 mL/h is achieved under the following conditions: the open area of the solar water heater is 50 kPa, the humidifier pressure is 50 kPa, the solar intensity is 1123 W/ m^2, and the volume of water flow is 18 L h^{-1}.

Nada *et al.* (2015) investigated air conditioning and HDD systems using a vapour-compression refrigeration cycle. The system's performance was assessed using the refrigeration capacity, water rate of production, and compressor work /kg of produced water while varying the air mass flow rate, inlet air temperature, and specific humidity. According to this study, the airflow rate and specific humidity were increased, resulting in improved performance in terms of the performance indices. Mohamed *et al.* (2020) created a mathematical model of an HDD system using cellulose paper as a packaging material for humidifiers in combination with solar panels, validated by experimental studies. The study concluded that the system provided water productivity of 2.45 kg h^{-1} at a unit cost of $ 0.047.

The current investigation will focus on developing a simulation programme (model) to simulate a desalination process using a polypropylene hollow-fibre membrane. Some important operating parameters, such as air flow velocity, temperature, flowrate, and salinities of feed water, were considered. The simulation programme will yield the temperature profiles and fluxes. An experimental setup was proposed with its components to allow varying operating parameters and finally to compare the setup results with the simulated predicted ones.

2. System Description and Experimental Setup

2.1. System Description.

To imitate the properties of seawater, the proposed system makes use of a synthetic solution of sodium chloride that has a concentration from 35000 mg L^{-1} to 150 g L^{-1}. This solution is monitored using a Kern Salt Refractometer. The humidification chamber makes use of polypropylene HF membrane bundles, each of which has pores measuring 0.1 x 0.5 micrometres. Under carefully monitored and regulated circumstances, the environmental chamber has a fan that expels air (temperature and humidity). There is a transfer of both heat and mass between the air on the shell-side of the HF membrane humidifier and the hot salty water that is moving through the fibre packs of the humidifier. In the presence of transmembrane vapour partial pressure differences, water vapour from the salty water contained inside the fibres can permeate through the pores of the membrane. Because the water vapour is transported out of the fibre by the airflow, the exit air gets warm and humid, whilst the salty water output becomes colder and somewhat more salinized as a result. The warm, muggy air forms condensation on the walls of the shell and tube heat exchanger

dehumidification unit and the freshwater that forms as a result is collected in the freshwater tank. The new hot salty water that has been produced by the heat exchanger is then merged with the hot, humid air that has been produced by the dehumidification unit, pumped into a stainless-steel tank, and heated even further by an immersion heater to the desired temperature (40–70 ^{o}C). Only after this process is complete is the mixture allowed to enter the dehumidification unit. A process flowchart is shown in Figure 1, which represents the experimental set-up.

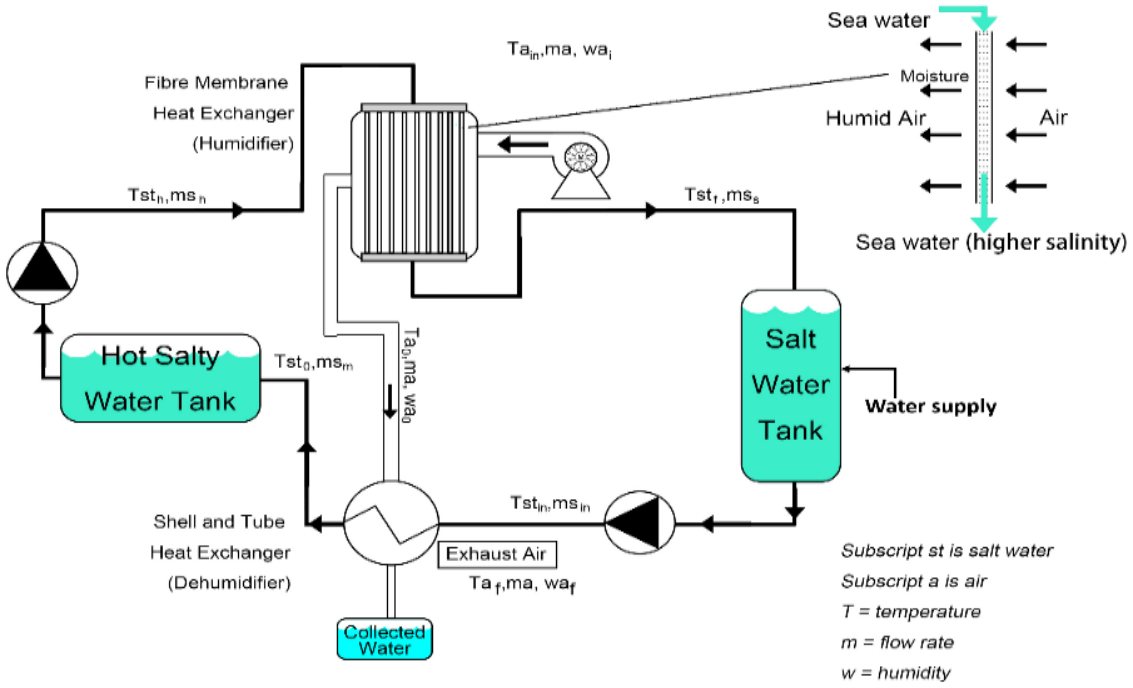

Figure 1. Proposed process schematic.

2.2. Experimental Setup

The experimental investigation aims to improve the system's performance by using various salty water and airflow rates. The humidification chamber comprises 18 bundles of HF membranes supplied by Zena company, Czech Republic, with 1385 fibres /bundle (Table 1 shows the HF membrane manufacturer specifications), a dehumidification chamber of a shell, and a tube heat exchanger is used. Subsequent initial heating in the shell tube heat exchanger, salty water is heated with an immersion heater to the required temperature. Dual Grundfos pumps circulate the salted water; the first pump circulates the cold salty water storage tank to the shell and tube heat exchanger, while the second pump circulates the hot salty water from the storage tank immersion heater to the humidification unit. The humidification chamber maintains continuous air circulation using an in-line ducted fan with a speed controller ambient temperature. Liquid flow rates are monitored by Atrato Ultrasonic Flow Meter.

Using the Sensirion EK-H4 assessment kit, it was able to determine the relative humidity and temperature of the air at several different locations around the system. Using thermocouples, the temperature of the air and the salty water was measured at several separate places, and the findings were logged into a data logger (Data Taker DT85). The experimental setup that was developed is given in Figure 2. The environmental chamber, which serves as the source of air,

has its temperature and relative humidity originally adjusted to 26 degrees Celsius and 65 per cent, respectively, for every test. Before commencing the process, the temperature of the immersion heater in the tank made of stainless steel is brought up to 70 degrees Celsius. After that, the system was operated for one full hour at the flowrates of both air and salty water. At the humidification chamber's outflow, temperature and relative humidity levels were monitored at the rate of one measurement per second. The regulated ambient temperature was taken from the environmental chamber. The temperature of the salty water was measured and recorded at the input of the humidification chamber, the outflow of the stainless-steel tank, and the dehumidification chamber every second. While keeping the flow rate of the salty water at a constant value of 0.05 metres per second, the ambient airspeed at the intake changed from 0.4 metres per second to 1.4 metres per second.

Table 1. Hollow-fibre membrane specifications

Property	Specification and value
Material	PP, Polypropylene
Pore size	0.1 µm average
Typical flux	150 L $m^{-2}h^{-1}$@1bar and 15 °C
OD / ID	310 / 240 µm
Surface treatment	Non-hydrophobic
Fibre burst pressure	> 5.5 bar
fibre collapse pressure	> 3.5 bar
Strength	2 N/fibre
Active surface area/bundle	0.9 m^2
pH resistance	2-11
Port connection	PVCu pipe 20mm
Standard length	750 ± 5mm

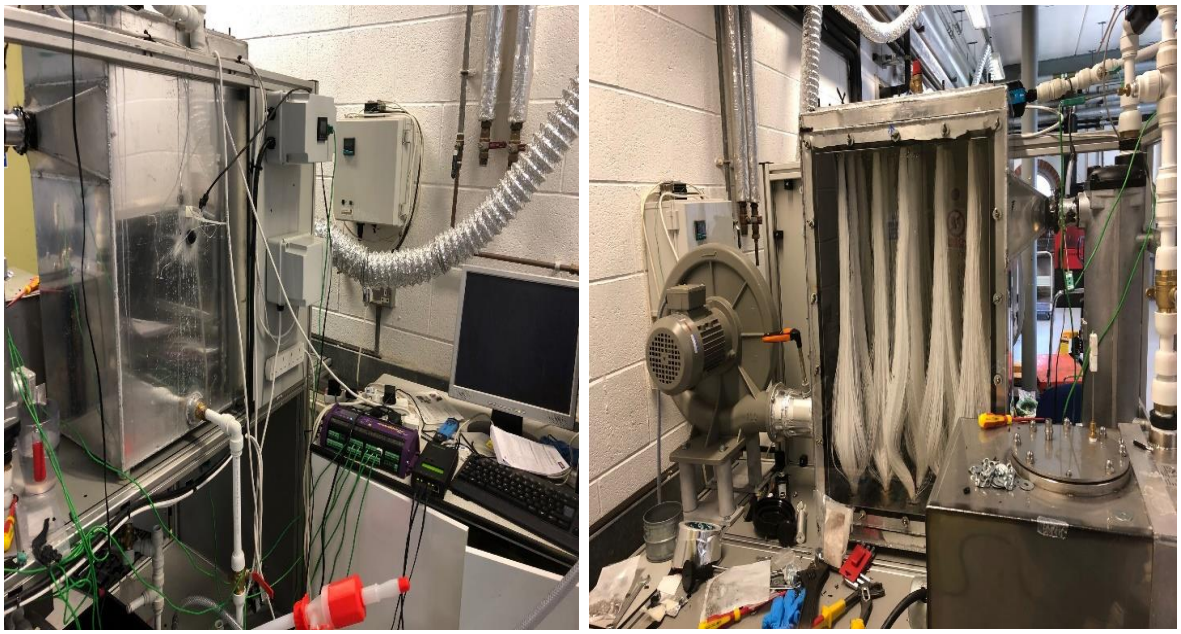

Figure 2. The system of the experimental test rig.

3. Mathematical Model

3.1. Theoretical Approach

For simulating the performance of the hollow-fibre membrane module, a finite-difference model was used. This model consisted of linked energy and mass balances. To represent the process of heat transmission in the bundled membrane fibres, a fractal technique was applied. Due to the interconnectedness of nearby fibres, single-fibre representations were deemed unreliable and hence disregarded. The following reductions in complexity were implemented:

(i) The performance of the module was consistent and adiabatic. (ii) There was hardly any loss of heat or mass in the axial direction. (iii) The module only had a one-dimensional flow pattern that was laminar for both gases and liquids. (iv) a tiny amount of water was present in the air stream that entered the module, and the pervaporation rates were low in comparison to the brine flow rate. This allowed the brine flow to be unaffected by the module's location. (v) The amount of water present in the air stream entering the facility was insignificant.

3.2 Modelling Strategy

Using the calibrated model, the following is a summary of the technique for modelling module performance in terms of (i) temperature profiles and (ii) total water production rate:

i. The simulation's boundary values included the molar flow rates of the brine and dry air that were being fed into it, the temperatures of the gas and liquid streams that were being fed into it, and a starting value that was supposed to be the temperature of the brine that was being discharged (Figure 3).

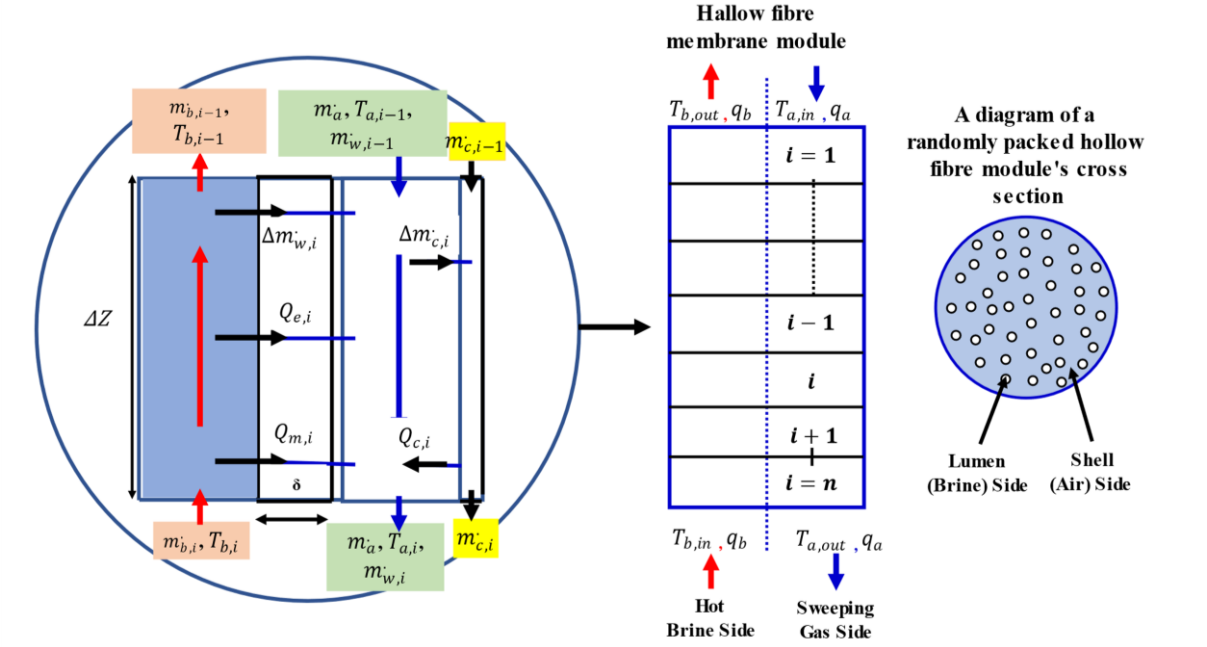

Figure 3. Magnified section of hollow fibre membrane

Figure 3 illustrates the mass and energy balances by magnifying a membrane fibre and its surroundings by ΔZ. Local mass balance control volume is the right-side dashed square. $\Delta m_{w,i}$ is the membrane's molar water vapour transport rate, $Q_{m,i}$ is the membrane's energy transfer rate, $Q_{c,i}$ is the air side's condensation rate, and $Q_{e,i}$ is the liquid stream's evaporation rate. Section molar water vapour condensation rate is $\Delta m_{c,i}$. T_a is the air

temperature, T_b is the brine temperature, $\dot{m}_c$ is the molar water condensation rate, $\dot{m}_w$ is the molar water rate of vapour at each section, $\dot{m}_b$ is the molar brine rate, $\dot{m}_a$ is the molar air rate, and q_a and q_b are the air and brine volumetric flowrates, respectively.

ii. Starting at the top (exiting brine effluent and air inlet), the counterflow module was analysed section by section using discretized forms of mass and energy balances to determine local rates of transmembrane water and energy transfer, local gas- and liquid-phase temperatures, and the partial pressure of water in the gas phase entering the next section. This was done to calculate the transmembrane water and energy transfer rates at specific locations. (Figure 4).

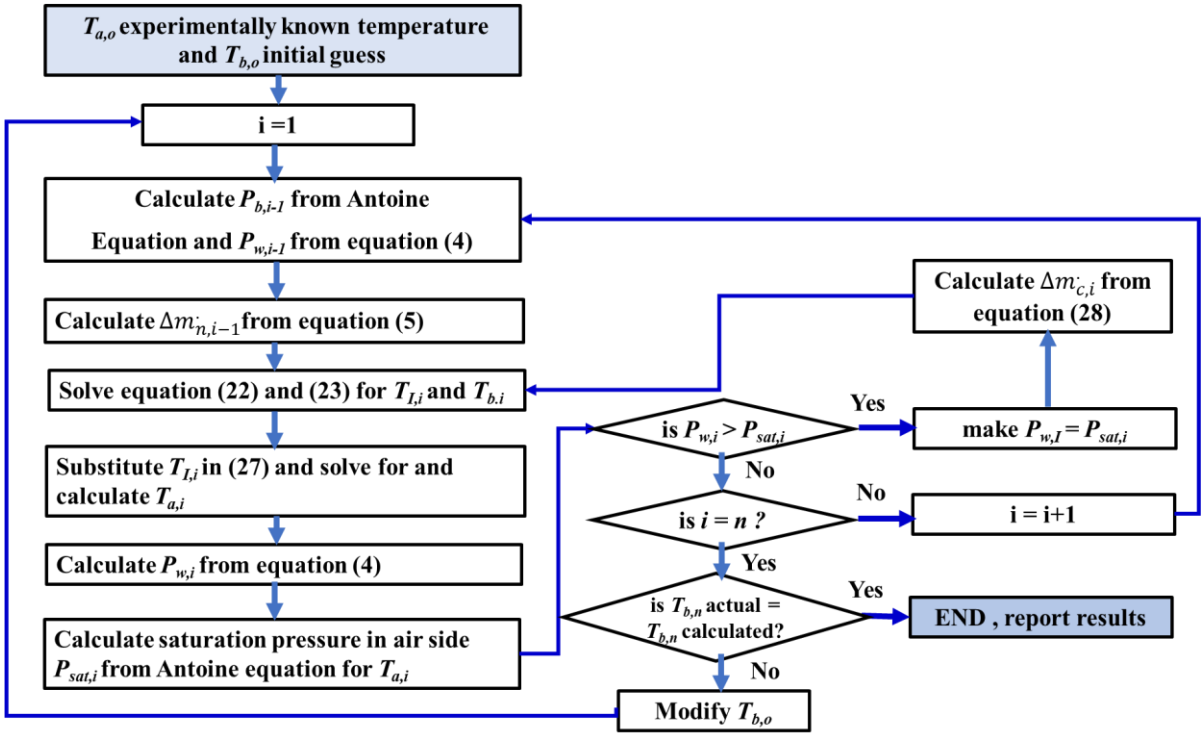

Figure 4. Algorithm of calculations

iii. After calculating the molar rate of water vapour transfer from liquid to gas (w), which was needed in the subsequent portion of the module to calculate the partial pressure of water, we moved on to the next step.

iv. Water partial pressure, temperature, and other variables were profiled in a series of profiles until the water partial pressure was close to its vapour pressure in the gas phase. Following that point, condensation of water vapour on the gas side of the membrane occurred to maintain a constant local vapour pressure. Condensation added to the energy balance of the column at the locations where it occurred, since heat was released during the process.

v. At the module's last step, the predicted brine temperature was compared to the actual brine temperature injected into the system. If it was more than 1% of the recorded temperature of the influent brine in degrees Celsius, the value estimated for the brine departing the system was adjusted by 0.5 degrees Celsius in the opposite direction of the mistake, and the stepwise calculations were restarted. The procedure was deemed finished once the threshold was met

3.3. Mass balance for hollow fibre membrane

The hollow-fibre membrane module for air humidification is essential in the whole HDD system. The fibre-to-fibre modelling is not likely, considering that there are numerous fibres. To ease the problem, simplified mass balances governing equations in the gas-control volume at each section *i* can be written as follows:

$$\dot{m}_{w,i} + \Delta\dot{m}_{c,i} = \dot{m}_{w,i-1} + \Delta\dot{m}_{w,i} \quad (1)$$

$$\dot{m}_a = \frac{p_{tot}}{RT_a} q_a \quad (2)$$

$$\dot{m}_{c,i} = \dot{m}_{c,i-1} + \Delta\dot{m}_{c,i} \quad (3)$$

where $\dot{m}_{w,i-1} and\ \dot{m}_{w,i}$ (mol min^{-1}) are the molar water vapour transport rates exit and entrance, respectively, $\Delta\dot{m}_{w,i}$ (mol min^{-1}) is the molar water vapour rate of transport across the membrane, $\Delta\dot{m}_{c,i}$ (mol min^{-1}) is the molar water vapour condensation rate in the section, $\dot{m}_a$ (mol min^{-1}) is the dry air molar transport rate, and q_a (m^3 min^{-1}) is the airflow rate of the sweeping gas. Values for the gas flowrate (q_a), temperature (T_a) in K and pressure (p_{tot}) in kPa were measured at the exit of the permeate tank.

The water vapour partial pressure in the gas phase, $P_{w,i}$ (atm) is obtained from:

$$P_{w,i} = \frac{\dot{m}_{w,i}}{\dot{m}_a + \dot{m}_{w,i}} P_{tot} \quad (4)$$

where $\dot{m}_a$ is the constant inlet molar flow of air, computed using the ideal gas law at each module stage. The movement of water vapour to the gas side was explained in each section *i* as follows:

$$\Delta\dot{m}_{w,i} = A_i J_i \quad (5)$$

where A_i is the inner interfacial surface area section (m^2), and J_i represents the transmembrane flux of water vapour through membrane pores (m^2) and can be calculated as follows.

$$J_i = \frac{k_{tot}}{RT}\left(P_{b,i} - P_{w,i}\right) \quad (6)$$

where k_{tot} is the total water vapour mass transfer coefficient (m s^{-1}), R is the gas law constant (8.205×10^{-5} m^3 atm K mol^{-1}), T is the interfacial brine temperature at the pore (K), $P_{b,i}$ is the vapour pressure computed using Antoine's equation (atm), and $P_{w,i}$ is the product of the mole fraction of water vapour in the sweep gas (atm).

From the saline side to the airside, the entire mass transfer resistance R_{tot} and coefficient K_{tot} can be calculated by Zhang (2011):

$$R_{tot} = \frac{1}{K_{tot}} = R_m + R_a = R_m + \frac{1}{k_a} \quad (7)$$

where R_m is the resistance to water vapour transport across the membrane, R_a is the resistance to mass transport in the air-side boundary layer, and k_a is the mass transfer coefficient on the airside of the membrane. The R_m can be formulated as:

$$R_m = R_{kn} + R_{mol} \quad (8)$$

which is given by Bennett (1952):

$$R_m = \frac{d_{inner}}{2\,D_{eff}} \ln\left[{d_{outer}}/{d_{inner}}\right] \quad (9)$$

where d_{outer} is the outer diameter of the HF membrane (m), d_{inner} is the HF inner diameter of the membrane (m), and D_{eff} is the effective water vapour diffusivity in the membrane (m^2 s^{-1}). In a porous membrane, the effective water vapour diffusivity is comparative to membrane porosity, ε, and inversely related to the effective tortuosity of routes through the membrane, τ, as can be formulated as follows:

$$D_{eff} = \frac{\varepsilon}{\tau} D \quad (10)$$

The relative significance of molecular diffusion and Knudsen endurance to R_a is determined by the effective pore size of the membrane. That is to say:

$$\frac{1}{D} = \frac{1}{D_{mol}} + \frac{1}{D_{Kn}} \quad (11)$$

where D_{mol} (m^2 s^{-1}) is estimated from Bennett (1952):

$$D_{mol} = \frac{0.926}{10^6\,P_{tot}} \left(\frac{T^{2.5}}{T + 245}\right) \quad (12)$$

where the P_{tot} is the total local pressure (kPa), T is the temperature of the feed side solution (K), and the D_{Kn} ($m^2 s^{-1}$) can be calculated using the following equation:

$$D_{Kn} = \tfrac{2}{3} r_P \left\lfloor \frac{8RT}{\pi m_w} \right\rfloor^{1/2} \quad (13)$$

where r_P is the pore radius (m), T is the brine temperature at the module's entrance (K), and m_w is the molecular water mass (kg mol^{-1}).

Herein, there are a few notions that must be established first as follows (Lawson and Lloyd, 1996):

$$N\left(\frac{d_{outer}}{d_{inner,m}}\right)^{Df} = 1 \quad (14)$$

where Df is the fractal dimension of the fibre packing, which represents the degree of non-uniformity in the distribution of the fibres $d_{inner,m}$ is the inner diameter of the module, and N is the number of fibres in the module (m). Furthermore, the packing density (φ) of a 2-dimensional element or the total cross-sectional area of the fibres to the module ratio can be given by:

$$\varphi = \left(\frac{d_{outer}}{d_{inner,m}}\right)^2 N \quad (15)$$

The hydrodynamic diameter of the module (shell side) can be formulated as:

$$d_h = \left(\frac{d^2{}_{inner,m} - N d^2{}_{outer}}{N d_{outer}}\right) \quad (16)$$

From the Sherwood number, the mass transfer coefficient k_a can be determined by:

$$k_a = \frac{D_{mol}\,Sh}{d_h} \quad (17)$$

The Sherwood number was calculated using empirical equations and tailored correlations specific to the hollow-fibre module form. The following correlations are based on a fractal relationship between the Sherwood number and the fractal dimension, with the laminar flow as the only constraint. The Sherwood number was derived using empirical formulae and fitted correlations specific to the hollow-fibre module (Zhang and Huang, 2011). With laminar flow as the only constraint, the following correlations are based on a fractal relationship between the Sherwood number and the fractal dimension, D_f as follows:

$$Sh = 14.06\varphi^4 - 29.21\varphi^3 + 22.59\varphi^2 - 7.71\varphi + 1.03Re^{0.33}Sc^{0.33}\psi_k \quad (18)$$

$$\psi_k = 0.882\, D_f - 0.535 \quad (19)$$

The mass transfer coefficient adjustment factor is ψ_k. The model has been validated under the following conditions: $1.6 \leq D_f \leq 1.9$ and $0.1 \leq \varphi \leq 0.8$. Moreover, The Reynolds number (Re) and Schmidt's number (Sc) are calculated using the following formulations:

$$Re = \frac{u_a d_h p_b}{\mu_v} \quad (20)$$

$$Sc = \frac{\mu_v}{P_b D_{mol}} \quad (21)$$

3.4. Energy balance in a single segment

In order to compute temperatures as a function of location within the brine and air streams, heat balances in both the brine-side and air-side portions were employed (Figure 3). On the brine side, up to the surface of the membrane, the energy balance is as follows:

$$m_b C_{P,b}\left(T_{b,i} - T_{b,i-1}\right) = h_w A_i N\left(T_{b,i} - T_{I,i}\right) \quad (22)$$

The rate of energy transfer from the brine to the membrane (brine side) is represented by the two sides of the following equation: where b (mol s^{-1}) is the molar brine flow, $C_{P,b}$ (Jmol^{-1} K^{-1}) is the specific heat of the brine, $T_{b,i}$and $T_{b,i-1}$ (K) are the brine outlet and input temperatures, respectively. The water's heat transfer coefficient, h_w (W K^{-1} m^{-2}), the inner area of a fibre section, A_i (m^2), the number of fibres, N, and the interfacial temperature, $T_{I,i}$ (K), are all inputs in this equation.

The energy transferred from the membrane interface to and through the membrane can be described by:

$$h_w A_i N\left(T_{I,i} - T_{b,i}\right) = Q_{m,i} + Q_{e,i} \quad (23)$$

The rate of heat transmission, denoted by $Q_{m,i}$ (W), across the membrane section is given by:

$$Q_{m,i} = h_{tot} A_o N(T_{I,i} - T_{a,i}) \quad (24)$$

Here, $T_{I,i}$ and $T_{a,i}$ are the pore and air temperatures of the brine interfacial membrane, respectively; h_{tot} (W K^{-1} m^{-2}) is the overall transmembrane heat transfer coefficient from the membrane to the air side (see below); and A_o (m^2) is the outer area of fibre in the section.

$$Q_{e,i} = \Delta \dot{m}_{w,i} \dot{\Delta} H_{v,w} \quad (25)$$

where $Q_{e,i}$ (W) is the rate at which heat is provided to evaporate liquid water from the brine stream, $\Delta m_{w,i}$ (mol s^{-1}) is the rate of vapour or permeate production, and $\Delta H_{v,w}$ is the latent heat of evaporation of water in J kg^{-1}, which is calculated from a correlation (El-Dessouky

and Ettouney,2002). In this equation, $Q_{e,i}$ (W) is the rate at which heat is provided. Taking T in Celsius:

$$\Delta H_{v,w} = (2501.9 - 2.41T + 0.0019T^2 + 0.00016T^3)10^{-3} \quad (26)$$

By rearranging equation (22) to solve for $T_{I,i}$, inserting equations (24) and (25) into (23) and then solving for the brine temperature at the exit from section i one may determine the temperature that is entering the subsequent module section.

The equilibrium of thermal energy on the air side is provided by equation (27), and it is connected to the equilibrium of heat on the brine side by the addition of $Q_{m,i}$ which equals the rate of heat transfer over the membrane (equation (24)).

$$\dot{m_a} C_{P,a}(T_{a,i-1} - T_{a,i}) + \dot{m_{w,\iota-1}} C_{P,v}(T_{a,i-1} - T_{a,i}) + \Delta\dot{m_{w,\iota}} C_{P,v}(T_{a,i-1} - T_{a,i}) = Q_{m,i} + Q_{c,i} \quad (27)$$

where $C_{P,a}$ (J mol^{-1} K^{-1}) is the gas-phase specific heat, $T_{a,i}$and $T_{a,i-1}$ (K) are the inlet and outlet gas-phase temperatures at section i and $C_{P,v}$ is the heat capacity of water vapour in J mol^{-1} K^{-1}. $T_{a,i}$ is the temperature at the inlet, and $T_{a,i-1}$ is the temperature at the exit. The amount of heat that is released as $Q_{c,i}$ (W) is determined by the condensation of water vapour in the section.

$$Q_{c,i} = \Delta H_{v,w} \Delta\dot{m}_{c,\iota} \quad (28)$$

where $Q_{c,i}$ is the rate of vapour condensation in the air stream, which only occurs under oversaturated circumstances, and $\Delta H_{v,w}$ (J kg^{-1}) is the latent heat of vaporisation, which is determined by using the equation. where $\Delta\dot{m}_{c,\iota}$ is the rate of vapour condensation in the air stream (26).

A system of four equations containing four unknowns is represented by equations (22), (23), (24) and (27). When equations (22), (24), and (28) are substituted into equation (27), and the air temperature at the exit from section i-1 is solved, we can get the air temperature at the beginning of the next section.

The complete membrane thermal transfer coefficient h_{tot} is given by (Becker, 2014):

$$\frac{1}{h_{tot}} = \frac{1}{h_a} + \frac{\delta}{\lambda_{eff}} \frac{d_{inner}}{2} ln\left(\frac{d_{outer}}{d_{inner}}\right) \quad (29)$$

where ha is the heat transfer coefficient on the airside of the membrane (W K^{-1} m^{-2}), δ is the membrane thickness (m), and λ_{eff} is the effective thermal conductivity of the membrane (W K^{-1} m^{-1}) and can be calculated as (Datta, 2007):

$$\lambda_{eff} = \lambda_v \epsilon + \lambda_m (1 - \epsilon) \quad (30)$$

The values of h_a and h_w were calculated as follows using the Chilton-Colburn analogy (Zhang and Huang, 2011):

$$h = \frac{\lambda\, Nu}{d} \quad (31)$$

The thermal conductivity of air (λ_v) and the hydrodynamic diameter of the shell side d_h (m) are used to calculate h_w (W K^{-1} m^{-2}). The Nusselt number can be calculated by the following formula: The thermal conductivity of water (λw) and the diameter of the lumen side are utilized to get h_w (W K^{-1} m^{-2}).

$$Nu = Sh.\, Le_{fl}^{1/3} \quad (32)$$

where the Sherwood number (Sh) for the shell side was calculated using equation (18) and the lumen side can be determined by the following formulation:

$$Sh = 1.62\left(\frac{d^2{}_{inner}U_b^2}{LD_{w,i}}\right)^{1/3} \quad (33)$$

where U_b is the brine approach velocity on the lumen side of the module (m s^{-1}), L is the fibre length (m) and $D_{w,i}$ is the liquid water diffusivity (m^2s^{-1}). The Lewis number, Le, is obtained as follows:

$$Le = \frac{Sc}{Pr} \quad (34)$$

Whereas the Pr can be calculated as:

$$Pr = \frac{\mu_v C_p}{\lambda_v} \quad (35)$$

4. Experimental and modelling results and discussions

Two separate experiments were conducted to determine the effects of varying the flow rates of salty water and the variable speed of air flowing from the environmental chamber. These were done in order to modify the temperature and humidity levels at the location where the results were analysed. The flux of freshwater that was generated throughout the testing ranged anywhere from 2.36 kg $h^{-1}m^{-2}$ to 10.6 kg $h^{-1}m^{-2}$ at 40°C and 70°C respectively. The quality of the water that was generated was evaluated, and the results indicated that it had values of electrical conductivity of 15 µS m^{-1} and 10 mg L^{-1}, which is comparable to the value of distilled water. Variation in salty water flowrates. Permeate flux rose with brine temperature and decreased with brine ionic strength, although marginally (Figure 5).

In light of the Causius-Clayperon equation, the effects of both variables can be understood in terms of the connections they share with the brine vapour pressure. The difference in pressure between the brine vapour pressure and the bulk partial pressure of water vapour in the same fibre section is what drives the transmembrane transfer of water (Equation (6)) in module simulations. This difference is measured in the same fibre section. The water temperatures at locations between the brine intake and outflows were not measured; rather, a mathematical model was used to determine the local water temperatures and vapour pressures. In spite of this, when the membrane pore tortuosity was the only fitted parameter, there was a strong correlation between predicted and actual permeate flow rates across a wide variety of experimental situations (Figures 5–7). Figure 5 shows the relationship between the vapour pressure of brine and the flux. Triangles were made by changing the concentration of NaCl in the brine (as shown) at 70 °C, U_a = 0.55 m s-1, and U_b = 0.05 m s^{-1}.

When a model is applied, it makes a solid line. The vapour pressure of the brine was most affected by the changes in temperature and ionic strength. The modelling work determined that temperature polarisation was quite small. (The difference between the interface temperature at the membrane surface and the local brine temperature was less than 0.5% (°C)). The vapour pressure of NaCl solutions was determined by solving for the activity of water in NaCl solutions, which is given by

$$a_{water} = 1 - 0.5x_{NaCl} - 10x_{NaCl}^2 \quad (36)$$

where x_{NaCl} is the mole fraction of NaCl. We can then calculate the vapour pressure by using the (Lawson & Lloyd, 1996) equation:

$$P_{water} = (1 - x_{NaCl}).a_{water}.P^{DI}_{water} \quad (37)$$

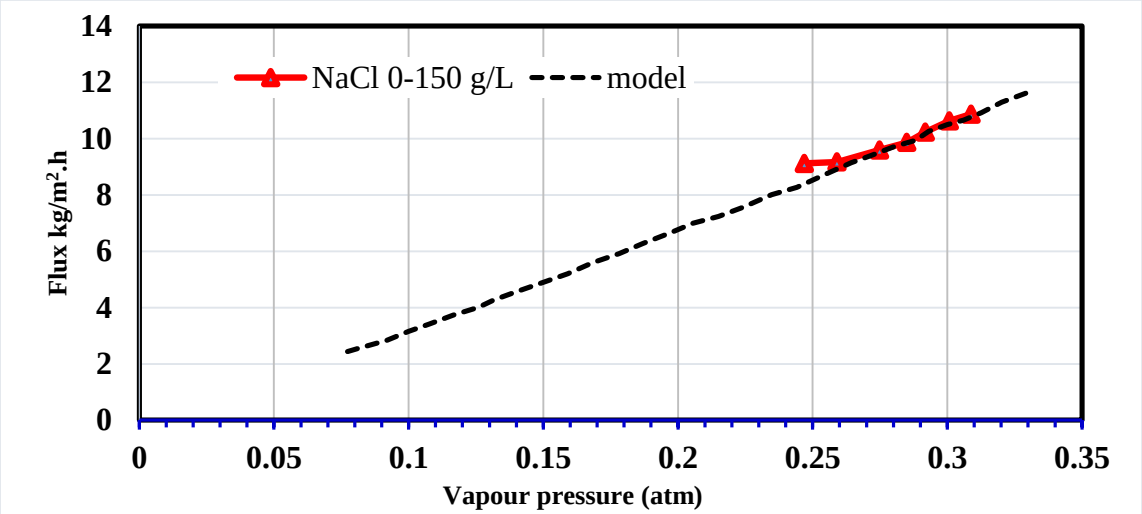

Figure 5. Relationship between the vapour pressure of brine and the flux.

Across the analysed operating condition range, both modelling and experiments show that permeate production is sensitive to brine temperature (Figure 6.). Unsurprisingly, there was little to no effect of changing the ionic strength of the brine across the range examined. At 140 g L^{-1} of NaCl, the rate of permeate formation was 23% lower than it was during the distillation of pure water. The concentration polarisation on the pore membrane surface only increased the local concentration by less than 0.3% estimated from (Martínez-Díez & Vázquez-González, 1999), hence it was disregarded. Concentrations of NaCl in the permeate were consistently below 5 mg L^{-1} throughout all trials.

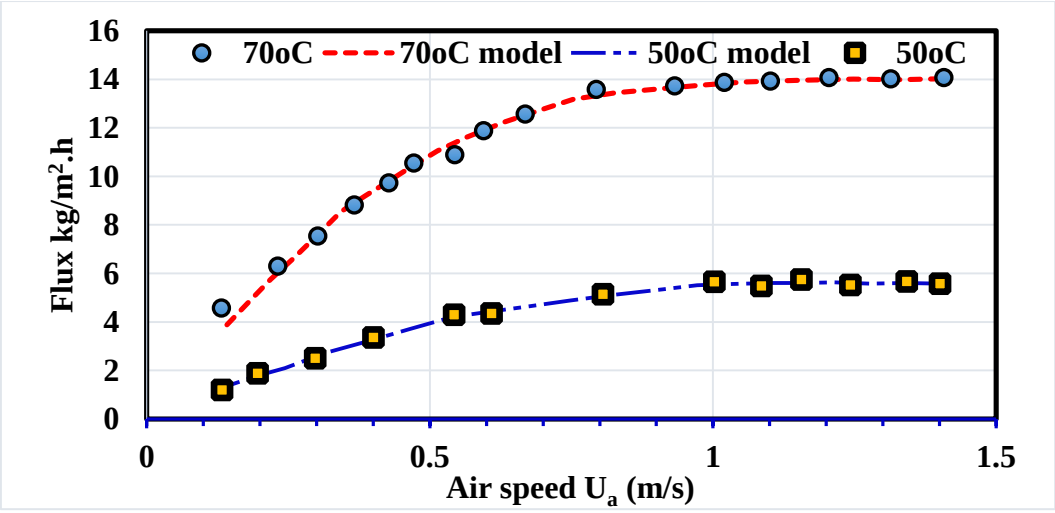

Figure 6. Water production rate (flux) vs sweep air velocity, U_a $(m\ s^{-1})$.

The accumulation of water vapour in the sweeping gas, as predicted by the saturation model, reduces the driving force for through-pore transport, which explains why the permeate collection rate decreases as the sweep air velocity increases. Exiting the module at a partial pressure of gas-phase water vapour close to the vapour pressure of water at the influent brine

temperature, the generation of permeate was found to be almost proportional to the gas flow rate (Figure 6). Nevertheless, at air flow velocities of 1.0 m s^{-1}, it is anticipated that the water collection rate would approach a transport-limited rate that is roughly proportionate to the brine vapour pressure.

The module's highest water purification rate is roughly 10.6 kg $m^{-2}h^{-1}$ at 70 ^{o}C and a flow velocity of 50 mm s^{-1} for the brine. While the highest rate of water purification should be nearly proportional to vapour pressure for the reasons described, module specifications prevented experimental measurement of water production rates at T > 80 ^{o}C. As the vapour pressure of water increases with increasing temperature, there is a strong motivation to create sweeping gas membrane distillation (SGMD) materials that can function at greater temperatures.

The math for straight lines is done. Brine flow velocities between 0.01 and 0.05 m s^{-1} at temperatures between 40 and 70 ^{o}C had insignificant effect on the observed and anticipated permeate flux (Figure 7). This indicates that the rate of water production was not drastically altered by the gradual decrease in brine temperature that occurred as the module progressed. There was a 23% variation in permeate collection rates between the lowest and highest brine flow velocities at the highest indicated influent brine temperature of 70 ^{o}C. The results of the simulated processes matched those of the experiments.

Permeate flux and temperature profiles may be used for design improvements since the model can accurately duplicate them throughout a wide variety of operating situations. Before anything else, the model elucidates the primary impediments to water vapour transfer through membranes.

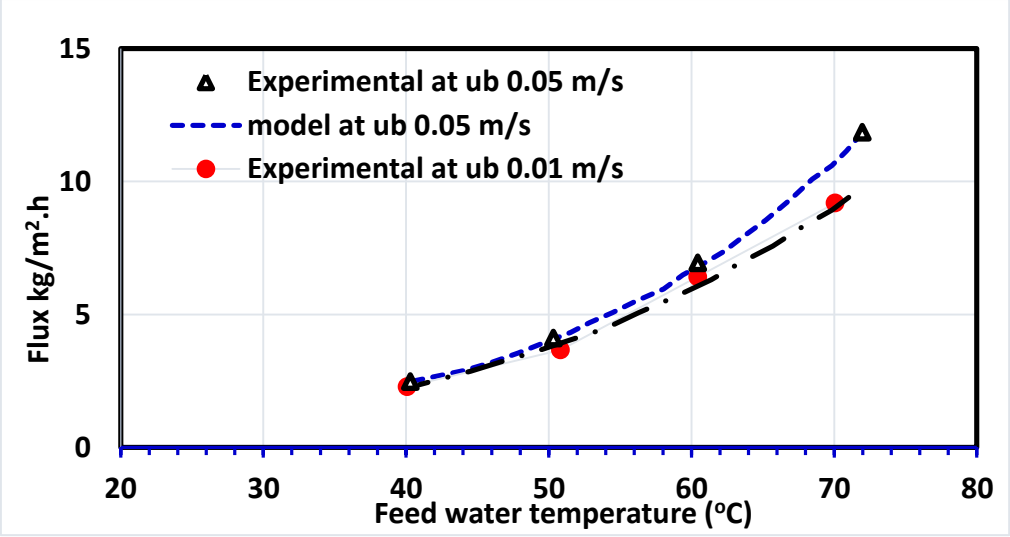

Figure 7. Relationship between feed water temperatures and a sweep air velocity

Lack of concentration polarisation leads to constant water activity, hence the resistance to water transport on the brine side of the membrane was disregarded. There are two sources of water vapour transport resistance across membranes: (i) molecular/Knudsen diffusion, and (ii) gas-phase transport through a concentration boundary layer on the shell side of the membranes (Figure 8). With a pore diameter of 0.26 µm and a gas velocity of 0.55 m s^{-1}, the resistance of the membrane is equivalent to the resistance in the gas phase boundary layer. The membrane's nominal pore size was 0.1 µm. Hence, over the range of air flow rates

studied experimentally, resistance to mass transfer across the gas-phase concentration boundary layer should play a somewhat lower role, but should not be disregarded. With a pore diameter of 0.15 µm, the Knudsen diffusion resistance is equivalent to the molecular diffusion resistance.

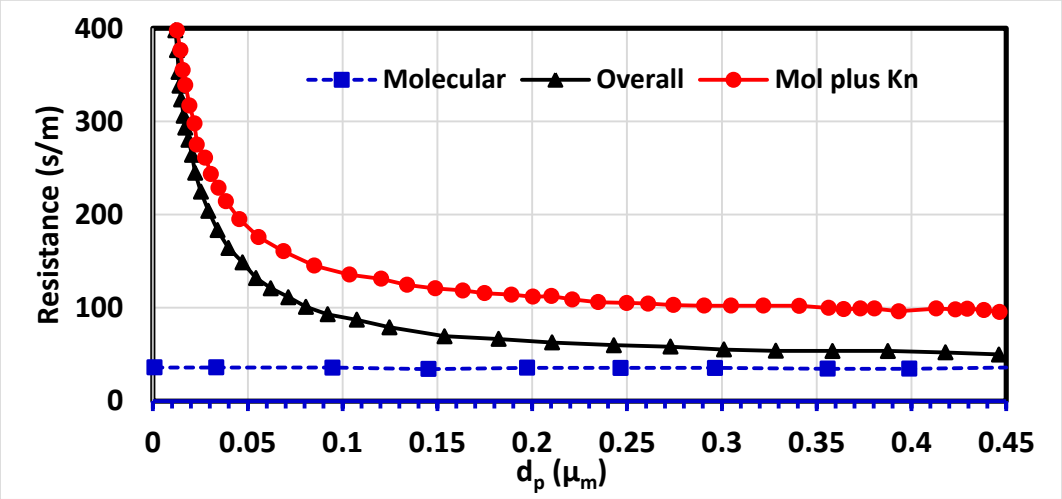

Figure 8. Mass transfer resistance R_{tot} versus membrane pore size at U_a = 0.55 m/s, T_b = 70°C, and U_b = 0.05 m/s.

The heat transfer resistance of brine was found to be negligible when compared to that of the gas phase boundary layer and membrane conduction. The computed values for h_w were 3079 W m^{-2} K^{-1}, h_m was 8.8 W m^{-2} K^{-1}, and h_a was 6.7 W m^{-2} K^{-1} for a brine temperature of T_b = 70 °C, U_a = 0.55 m s^{-1}, and U_b = 0.05 s^{-1}. Hence, the resistances of the air side and the membrane are the primary constraints on heat transmission.

The predicted water purification rate was unaffected by an increase in membrane pore size of about 5 times (from 0.1 µm to 0.45 µm) at temperatures between 40 and 70 degrees Celsius (Figure 9).

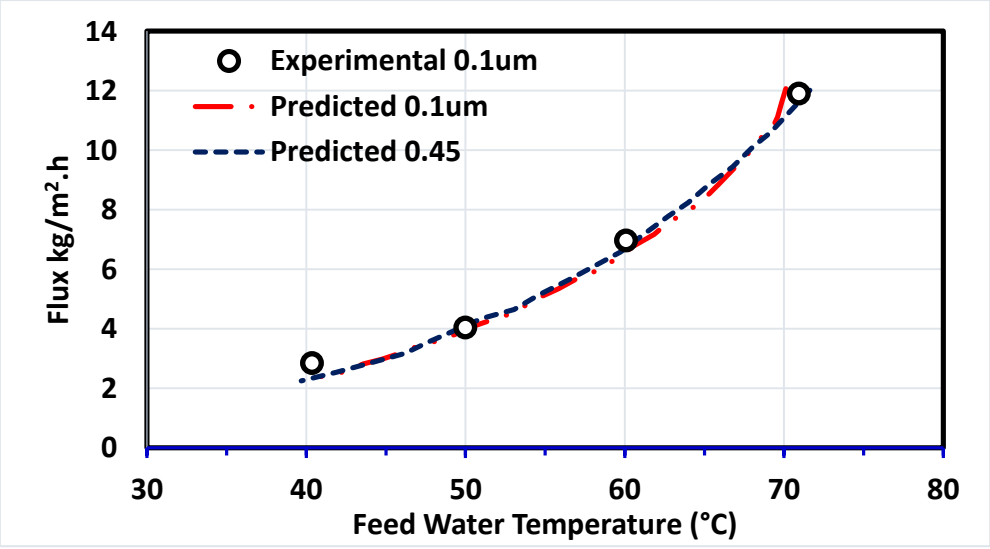

Figure 9. Flux versus changes with the temperature of the feed water

Figure 10 shows how the size of the pores in the membrane affects the partial pressure of water along the normalised length of the module when U_a = 0.55 m s^{-1} and U_b = 0.05 m s^{-1}, L_0 = 75 cm, and T = 70 °C at the brine inlet. Where x = 0 is the top of the module (where air

goes in and brine comes out) and $x = L_0$ is the bottom of the module (air out and brine in). The following explains why the SGMD water purification rate is not sensitive to membrane pore size. The gas stream was practically saturated with water vapour at the module exit in both instances, therefore the effluent gas-phase water content was just a 10% difference. This is despite the fact that the barrier to mass transfer is substantially lower for the large pore size membrane (Figure 10). Even though the Knudsen effects on the total mass transfer resistance were much reduced in the bigger pores, the module was long enough to bring the effluent air stream to near-saturation levels of water vapour. But, with substantially greater sweep air velocities, the larger-pore membrane should appear favourable.

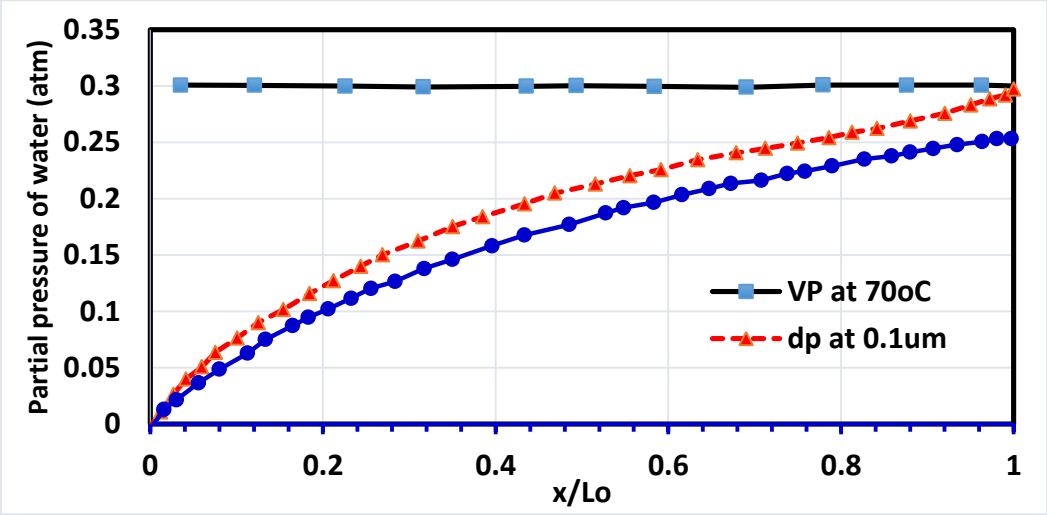

Figure 10. size of the pores in the membrane affects the partial pressure of water

5. CONCLUSIONS

For the purpose of predicting the amount of flux during SGMD using hollow fibre membrane modules, coupled heat and mass balances were created. The results of experimental testing verified the calculations throughout a wide range of sweeping air flow velocities as well as temperatures, flowrates, and salinities of the feed water. Using the verified model, we looked at how different values of effective membrane pore size, sweeping gas velocity, brine velocity, and temperature affected the anticipated water production rate beyond the range of the experimental equipment employed in this study (up to temperatures of 80oC).

The results of the model indicate that the resistance to mass transfer across the membrane is equivalent to the resistance to mass transfer on the air side of the membrane when the pore diameters of the membrane are 0.26 microns (U_a = 0.55 metres per second). When the pore diameters are bigger than 0.26 microns, the air side boundary layer is the primary cause of the constraints that are placed on mass transfer. Limitations in heat transport are typically caused by boundary layer effects on the air side of the system. The modelling also lends credence to the following hypotheses and conclusions:

- When sweeping gas velocities are relatively low, gas flow rate and water vapour pressure are often the limiting parameters for water production. At high air flow rates, the generation of water is constrained by the rate of mass transfer from brine to sweep air, which is essentially proportional to the vapour pressure of water, at least for the tiny pore membranes utilised in this study.

- An increase in membrane fibre length increases water production until the partial pressure of water vapour in the sweep gas approaches the vapour pressure of water in the membrane module.
- The flux is only sensitive to the membrane's pore size. The reasons for this are elucidated by simulations of modules that depend on the aforementioned variables and others.
- The temperature polarisation in the hollow fibre module was practically non-existent.
- The resistance to the transfer of mass, rather than the transfer of heat, was a significantly more crucial factor in determining the permeate flux.

In order to concurrently match the boundary temperatures (inlet and outlet) in the brine and gas flows, the risk of water recondensation within the module has to be considered. The incorporation of a recondensation term on the air side of the membrane resulted in significantly greater temperature variations over the length of the module for both the gas and brine streams. The insertion of a recondensation term on the air side of the membrane led to this result.

6. NOMENCLATURE

A_i	inner interfacial surface area section, (m^2)	$P_{b,i}$	vapour pressure, (atm)
d_{inner}	HF inner diameter of the membrane, (m)	$P_{w,i}$	product of the mole fraction of water vapour in the sweep gas, (atm).
$d_{inner,m}$	inner diameter of the module, (m)	P_{tot}	total pressure at the exit of the permeate tank, (kPa)
Df	fractal dimension of the fibre packing	q_a	airflow rate of the sweeping gas, (m^3 min^{-1})
d_{outer}	outer diameter of the HF membrane, (m)	R_m	resistance to water vapour transport across the membrane
D_{eff}	effective water vapour diffusivity in the membrane, (m^2 s^{-1})	R_a	resistance to mass transport in the air-side boundary layer
$D_{w,i}$	liquid water diffusivity, (m^2s^{-1}).	R	gas law constant, (8.205×10^{-5} m^3 atm K mol^{-1})
ha	heat transfer coefficient on the airside of the membrane, (W K^{-1} m^{-2})	r_P	pore radius, (m)
J_i	transmembrane flux of water vapour through membrane pores, (m^2)	Re	Reynolds number
k_{tot}	total water vapour mass transfer coefficient, (m s^{-1})	Sc	Schmidt's number
k_a	mass transfer coefficient on the airside of the membrane	Sh	Sherwood number
Le	Lewis number	T_a	air temperature, (K)
$\dot{m}_{w,i}$	molar water vapour transport rates at the entrance, (mol min^{-1})	T	temperature of the feed side solution, (K)
$\Delta\dot{m}_{w,i}$	molar water vapour rate of transport across the membrane, (mol min^{-1})	U_b	brine approach velocity on the lumen side of the module, (m s^{-1})
$\Delta\dot{m}_{c,i}$	molar water vapour condensation rate in the section, (mol min^{-1})	δ	membrane thickness, (m)
$\dot{m}_{w,i-1}$	molar water vapour transport rates exit, (mol min^{-1})	λ_{eff}	effective thermal conductivity of the membrane, (W K^{-1} m^{-1})
m_w	the molecular water mass, (kg mol^{-1})	ψ_k	mass transfer coefficient adjustment factor
$\dot{m}_a$	dry air molar transport rate, (mol min^{-1})	φ	packing density
N	number of fibres in the module	ε	membrane porosity

7. REFERENCES

Al-Otoom A. and Al-Khalaileh A.T. (2020) Water desalination using solar continuous humidification–dehumidification process using hygroscopic solutions and rotating belt. Solar Energy 197:38-49.

Arnot T. and Mattia D. (2011) A review of reverse osmosis membrane materials for desalination–development to date and future potential. Journal of Membrane Science.

Ayati E., Rahimi-Ahar Z., Hatamipour M.S. and Ghalavand Y. (2019) Water productivity enhancement in variable pressure humidification dehumidification (HDH) desalination systems using heat pump. Applied thermal engineering 160:114114.

Becker S. (2014) Foundations of heat transfer. von FP incropera, DP dewitt, TL bergman, AS lavine. Chemie Ingenieur Technik 3:395-396.

Bennett C. (1952) Absorption and Extraction. Thomas K. Sherwood and Robert L. Pigford. New York-London: McGraw-Hill, 1952. 478 pp. $7.50. Science 116:156-156.

Chen Q., Burhan M., Shahzad M.W., Ybyraiymkul D., Akhtar F.H. and Ng K.C. (2020) Simultaneous production of cooling and freshwater by an integrated indirect evaporative cooling and humidification-dehumidification desalination cycle. Energy conversion and management 221:113169.

Datta A.K. (2007) Porous media approaches to studying simultaneous heat and mass transfer in food processes. I: Problem formulations. Journal of Food Engineering 80:80-95.

El-Dessouky H., Shaban H.I. and Al-Ramadan H. (1996) Multi-stage flash desalination process: A thermal analysis. Developments in Chemical Engineering and Mineral Processing 4:5-22.

Elbassoussi M.H., Mohammed R.H. and Zubair S.M. (2020) Thermoeconomic assessment of an adsorption cooling/desalination cycle coupled with a water-heated humidification-dehumidification desalination unit. Energy conversion and management 223:113270.

Elzayed M.S., Ahmed M., Qasem N.A., Antar M.A. and Zubair S.M. (2020) A design procedure to size thermodynamically-balanced humidification-dehumidification desalination systems. Energy conversion and management 224:113357.

Faegh M. and Shafii M.B. (2020) Thermal performance assessment of an evaporative condenser-based combined heat pump and humidification-dehumidification desalination system. Desalination 496:114733.

Gabelich C.J., Williams M.D., Rahardianto A., Franklin J.C. and Cohen Y. (2007) High-recovery reverse osmosis desalination using intermediate chemical demineralization. Journal of Membrane Science 301:131-141.

He W., Chen J., Han D., Luo L., Wang X., Zhang Q. and Yao S. (2019a) Energetic, entropic and economic analysis of an open-air, open-water humidification dehumidification desalination system with a packing bed dehumidifier. Energy conversion and management 199:112016.

He W., Han D., Zhu W. and Ji C. (2018) Thermo-economic analysis of a water-heated humidification-dehumidification desalination system with waste heat recovery. Energy conversion and management 160:182-190.

He W., Yang H. and Han D. (2019b) Thermodynamic investigation and optimization of a heat pump coupled open-air, open-water humidification dehumidification desalination system with a direct contact dehumidifier. Desalination 469:114101.

Jabari F., Nazari-heris M., Mohammadi-ivatloo B., Asadi S. and Abapour M. (2020) A solar dish Stirling engine combined humidification-dehumidification desalination cycle for cleaner production of cool, pure water, and power in hot and humid regions. Sustainable Energy Technologies and Assessments 37:100642.

Lawal D.U., Antar M.A., Khalifa A., Zubair S.M. and Al-Sulaiman F. (2020) Experımental investigation of heat pump driven humidification-dehumidification desalination system for water desalination and space conditioning. Desalination 475:114199.

Lawson K.W. and Lloyd D.R. (1996) Membrane distillation. I. Module design and performance evaluation using vacuum membrane distillation. Journal of Membrane Science 120:111-121.

Lawson, K. W., & Lloyd, D. R. (1996). Membrane distillation. II. Direct contact MD. Journal of Membrane *Science*, *120*(1), 123–133. https://doi.org/10.1016/0376-7388(96)00141-X

Li G.-P., Qi R.-h. and Zhang L.-Z. (2019) Performance study of a solar-assisted hollow-fibre-membrane-based air humidification-dehumidification desalination system: Effects of membrane properties. Chemical Engineering Science 206:164-179.

Martínez-Díez, L., & Vázquez-González, M. I. (1999). Temperature and concentration polarization in membrane distillation of aqueous salt solutions. Journal of Membrane Science, 156(2), 265–273. https://doi.org/10.1016/S0376-7388(98)00349-4

Mohamed A., Ahmed M.S. and Shahdy A.G. (2020) Theoretical and experimental study of a seawater desalination system based on humidification-dehumidification technique. Renewable Energy 152:823-834.

Nada S., Elattar H. and Fouda A. (2015) Experimental study for hybrid humidification–dehumidification water desalination and air conditioning system. Desalination 363:112-125.

Pourafshar S.T., Jafarinaemi K. and Mortezapour H. (2020) Development of a photovoltaic-thermal solar humidifier for the humidification-dehumidification desalination system coupled with heat pump. Solar Energy 205:51-61.

Qasem N.A. and Zubair S.M. (2019) Performance evaluation of a novel hybrid humidification-dehumidification (air-heated) system with an adsorption desalination system. Desalination 461:37-54.

Rahimi-Ahar Z., Hatamipour M.S., Ghalavand Y. and Palizvan A. (2020) Comprehensive study on vacuum humidification-dehumidification (VHDH) desalination. Applied thermal engineering 169:114944.

Sachdev T., Gaba V.K. and Tiwari A.K. (2020) Performance analysis of desalination system working on humidification-dehumidification coupled with solar assisted air heater and wind tower: Closed and open water cycle. Solar Energy 205:254-262.

Sayyaadi H. and Saffari A. (2010) Thermoeconomic optimization of multi effect distillation desalination systems. Applied Energy 87:1122-1133.

Sharshir S., Peng G., Yang N., Eltawil M.A., Ali M.K.A. and Kabeel A. (2016) A hybrid desalination system using humidification-dehumidification and solar stills integrated with evacuated solar water heater. Energy conversion and management 124:287-296.

Shatat M., Omer S., Gillott M. and Riffat S. (2013) Theoretical simulation of small scale psychometric solar water desalination system in semi-arid region. Applied thermal engineering 59:232-242.

Shehata A.I., Kabeel A., Dawood M.M.K., Elazm M.M.A., Abdalla A.M. and Mehanna A. (2019) Achievement of humidification and dehumidification desalination system by utilizing a hot water sprayer and ultrasound waves techniques. Energy conversion and management 201:112142.

Teow Y.H. and Mohammad A.W. (2019) New generation nanomaterials for water desalination: A review. Desalination 451:2-17.

Wang N., Wang D., Dong J., Wang H., Wang R., Shao L. and Zhu Y. (2020) Performance assessment of PCM-based solar energy assisted desiccant air conditioning system combined with a humidification-dehumidification desalination unit. Desalination 496:114705.

Wang Z., Dou B., Zheng L., Zhang G., Liu Z. and Hao Z. (2012) Effective desalination by capacitive deionization with functional graphene nanocomposite as novel electrode material. Desalination 299:96-102.

Welgemoed T.J. (2006) Capacitive deionization technologyTM development and evaluation of an industrial prototype system, University of Pretoria.

Yang C.-M., Choi W.-H., Na B.-K., Cho B.W. and Cho W.I. (2005) Capacitive deionization of NaCl solution with carbon aerogel-silicagel composite electrodes. Desalination 174:125-133.

Zhang L.-Z. (2011) An analytical solution to heat and mass transfer in hollow fibre membrane contactors for liquid desiccant air dehumidification. Journal of heat transfer 133.

Zhang L.-Z. and Huang S.-M. (2011) Coupled heat and mass transfer in a counter flow hollow fibre membrane module for air humidification. International Journal of Heat and Mass Transfer 54:1055-1063.

Zhang L.-Z. and Li G.-P. (2017) Energy and economic analysis of a hollow fibre membrane-based desalination system driven by solar energy. Desalination 404:200-214.

محاكاة تحلية المياه المالحة باستخدام أغشية من الياف البولي بروبلين المجوفة

د/ محمود محمد عليوه[١]، د. عمر رمضان[٢]، د/ محمود الامام[٣]، د/ عبد العزيز ابراهيم عماره[٤]

[١] استاذ مساعد الهندسة البيئية - الاكاديمية العربية للعلوم والتكنولوجيا والنقل البحري - الاسكندرية - مصر.
[٢] مدرس الهندسة البيئية - قسم العمارة والبيئة العمرانية - جامعة نوتنغهام - المملكة المتحدة.
[٣] مدرس هندسة القوى والآلات الزراعية - قسم الهندسة الزراعية والنظم الحيوية - ك. الزراعة - ج. الإسكندرية - مصر.
[٤] استاذ مساعد هندسة الري والصرف - قسم الهندسة الزراعية والنظم الحيوية - ك. الزراعة - ج. الإسكندرية - مصر.

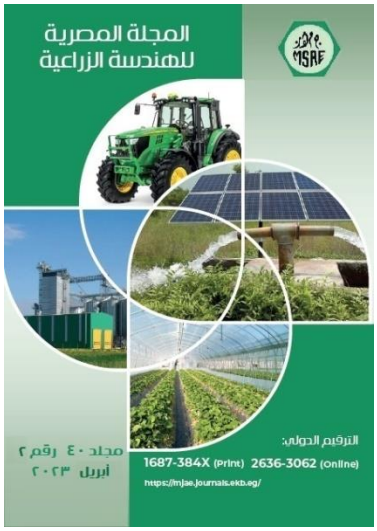

الكلمات المفتاحية:
تحلية المياه؛ الترطيب؛ إزالة الرطوبة؛ الأغشية المجوفة؛ برنامج محاكاه.

الملخص العربي

تعتبر تحلية المياه البحرية أو قليلة الملوحة حلا فعالا ومستداما لنقص المياه العالمي والزيادة السريعة في الطلب على المياه العذبة. في هذا السياق، تم فحص نظام تحلية المياه باستخدام أغشية الألياف المجوفة المتقدمة في غرفة الترطيب في مرفق الاختبار لترطيب وتسخين الهواء المحيط. وبالتالي، تم تبريد الهواء المرطب عن طريق نقل الحرارة في غرفة إزالة الرطوبة، والتي تكثف بخار الماء وتنتج مياه شرب عذبة عالية الجودة. تم تحضير مياه البحر المحاكية في المختبر لقياس إجمالي المواد الصلبة الذائبة (TDS) والتوصيل الكهربائي قبل وبعد عملية التحلية. كذلك تم تطوير برنامج رياضي لمحاكاة النظام (model). تم تقييم أداء اغشية الالياف المجوفة كوسيط مرطب للهواء المحيط باستخدام تدفقات كتلة مختلفة من الماء المالح والهواء لتحسين أداء تشغيل النظام. تم إجراء تجارب معملية لاختبار تأثير تغيير معاملات التشغيل على تدفق المياه العذبة المنتجة. حيث تراوح تدفق المياه الناتجة من ٢,٣٦ – ١٠,٦٠ كجم في ساعة لكل متر مربع عند درجات حرارة من ٤٠ – ٧٠ درجة مئوية، على التوالي. كما اتفقت نتائج برنامج المحاكاة مع النتائج التجريبية الي حد كبير وكذلك أظهر تحليل جودة المياه أن القيم التي تم الحصول عليها كانت تتبع إرشادات مياه الشرب الصادرة عن منظمة الصحة العالمية.